Experimental and numerical study of NO_x formation in a domestic H_2/air coaxial burner at low Reynolds number

G. Lopez-Ruiz[a,b], I. Alava[a], I. Urresti[a], J. M. Blanco[b], B. Naud[c]

[a] *Ikerlan Technology Research Centre, Basque Research and Technology Alliance (BRTA). P. J.M. Arizmendiarrieta, 2. 20500 Arrasate/Mondragón, Spain.*
[b] *School of Engineering Bilbao, University of the Basque Country (UPV/EHU), Plaza Ingeniero Torres Quevedo. Edif.I, Bilbao, 48013, Spain.*
[c] *Modelling and Numerical Simulation Group, Energy Department, CIEMAT, Avda., Complutense 40, 28040 Madrid, Spain*

Highlights

- Hydrogen is a potential fuel for domestic burners
- NO_x reduction can be achieved by flame splitting method
- Laminar and turbulent flames show opposite NO_x trends with increasing inlet powers
- In low Reynolds number flames lower equivalence ratios imply higher NO_x concentrations
- Competing factors describing local NO_x production intensity can be defined

Abstract

Thermal NO_x formation in H_2/air jet flames from a coaxial burner is studied experimentally and numerically. The aim is to study possible NO_x reduction strategies for domestic gas boiler burners. Following a flame splitting method strategy, a single burner is studied at different inlet powers (from 0.2 to 1.0 kW). The effect of three different fuel-air ratios (or equivalence ratio ϕ) is considered by varying the coaxial air stream, with fuel-air ratios corresponding to values of $\phi < 1$, relevant for domestic boiler applications (here $\phi = 0.77$, $\phi = 0.83$ and $\phi = 0.91$). NO_x concentrations increase with increasing inlet power between 0.2 and 0.6 kW and numerical results are in good correspondence with available experimental data. The opposite trend is observed above 0.6 kW and no numerical results are obtained, indicating a transition from laminar to turbulent flames. On the other hand, in contrast to the observations made in turbulent non-premixed flames, reducing the equivalence ratio implies higher NO_x concentrations in the low Reynolds number flames considered. The numerical results in the laminar regime are used to highlight and quantify three competing main factors concerning NO_x production in order to interpret the experimental observations: the volume of the region where NO_x is produced, and within this region, the competition between residence time and NO_x reaction rate. Based on this analysis, different design strategies for low NO_x hydrogen diffusion burners are finally discussed.

Keywords:
Domestic Burner, Hydrogen Economy, NO_x reduction, Flame splitting, Coaxial air, Laminar simulations

1. Introduction

Hydrogen is a potential alternative to fossil fuels in transportation, industrial, commercial and residential sectors [1, 2, 3]. Since hydrogen can be generated through different renewable energy sources [4, 5, 6], the so-called hydrogen economy could be an integral part of a renewable energy system, allowing the substitution of pipeline natural gas with renewable hydrogen to reduce carbon emissions as well as the dependence on fossil fuels [2, 7, 8]. The end use of this renewable hydrogen has been a research topic during the last decades. For instance, different studies focused on the use of generated renewable hydrogen as fuel in combustion devices such as internal combustion engines or burners [9, 10, 11, 12]. An extensive research literature on hydrogen flames can be found, since its combustion behaviour presents several particularities compared to other conventional gaseous fuels, due to its physical properties. Among others, hydrogen presents a wide flammability limit in air (4-75 vol%), low ignition energy in air (0.019 mJ), low density (0.0899 kg/m^3) and high adiabatic flame temperature (2380 K) [13, 14, 15, 16]. Hence, the variety of combustion devices in different sectors still requires an in-depth research work to re-adapt or re-design them so as to ensure safe and efficient operating conditions when using hydrogen as inlet fuel. In this context, the present study focuses on the use of gaseous hydrogen as fuel in domestic gas boiler burners. As discussed by de Vries *et al.* [17], while fundamental changes in combustion phenomena and exhaustive analysis of individual combustion devices has been widely studied, there is no clear conclusion concerning the maximum fraction of hydrogen that maintains the performance of installed domestic combustion appliances without adverse consequences.

The safety risk when burning hydrogen is closely related to the flame flashback phenomena due to the high flame front velocities in premixed and partially premixed flames, mainly caused by an imbalance in the local flame and flow speeds,

when the former exceeds the latter [18, 19, 20, 21]. Recently, Zhao *et al*. [22] studied the influence of hydrogen addition to pipeline natural gas on the combustion performance of a partially premixed cooktop burner. They concluded that the burner could operate safely and efficiently with a maximum hydrogen concentration of 20%. In addition, the measured NO$_x$ emissions were over 100 ppm, without meaningful variations when adding hydrogen. Similarly, Choudhury *et al*. [23] studied the admissible hydrogen percentage in natural gas in low-NO$_x$ and conventional water heaters, working with partially premixed and lean premixed conditions. They analyzed characteristics such as flashback, ignition delay, flame structure and emissions. The most interesting conclusion was that the maximum hydrogen tolerance in both low-NO$_x$ and conventional water heater was below 10% by volume.

On the other hand, many combustors operate in the non-premixed mode since they ensure safer operating conditions, avoiding flashback and explosion risks [15, 24, 25]. However, in hydrogen flames around atmospheric pressure as in the present study, where NO$_x$ formation can be correctly described by the well known Zeldovich mechanism or thermal mechanism [26, 27], the high adiabatic flame temperature of hydrogen diffusion flames (peak temperatures above 2300K in this study) can yield to high levels of NO$_x$ [28, 29, 30]. Therefore, the main technological challenge in the design of hydrogen burners is to maintain both a high hydrogen fuel content and acceptable levels of NO$_x$ emissions. This clearly requires new or modified existing combustion equipments for hydrogen. Non-premixed combustion can be considered to be the best option to design domestic hydrogen burners since they completely eliminate the flashback phenomena, and voluminous research has been published on turbulent non-premixed hydrogen burners. However, laminar non-premixed hydrogen burners have been hardly studied in the literature. We summarize here some relevant studies.

Igawa *et al*. [31] examined the effect of splitting hydrogen diffusion flames on NO$_x$ emissions for stove gas burners. The experimental setup had no confinement or combustion chamber for the flames, and hydrogen was mixed with the ambient air through diffusion. They recorded measurements at different nozzle diameters for individual and multi-flame burners (0.6, 1.2 and 2.6 mm) and at different nozzle intervals for multi-flame measurements. They also experimentally concluded that splitting the flame was an effective method to decrease NO$_x$ emissions in hydrogen diffusion flames, since they measured lower NO$_x$ emissions when dividing a single flame burner into three flames for the same total input power.

Chen and Driscoll [33] experimentally studied the effects of coaxial air and fuel jet Reynolds number on NO$_x$ formation in non-premixed jet flames. They aimed at deriving general scaling laws for NO$_x$ production (in methane/air and hydrogen/air flames, both with and without coaxial air, and both in laminar and turbulent flames). The results showed that coaxial air reduced NO$_x$ formation in hydrogen flames and had a negligible effect in methane flames at Re=5000. In addition, the results for simple hydrogen jet diffusion flames without coaxial air showed a reduction of NO$_x$ levels when reducing the hydrogen inlet diameter from 0.37 to 0.16 cm in both laminar and turbulent regimes. Their attempt to derive general scaling laws is interesting in order to higlight what we will consider here as the three main physical aspects that play a key role, and may compete, in NO$_x$ production:

1. following the Eulerian approach of Peters *et al*. [34], they related the production of NO$_x$ to a reaction volume $\mathcal{V}_{\text{reac}}$ (proportional to $L_f^2.\delta$, where L_f is the flame length and δ the flame thickness);

2. from a Lagrangian point of view, they pointed out how the relevant dimension is a residence time τ_{res} (within $\mathcal{V}_{\text{reac}}$);

3. they also indirectly considered the chemical time of NO$_x$

production (i.e. the inverse of a reaction rate $\dot{\omega}_{NOx}$).

Keeping this in mind, the following references are interesting since they give some insight on these factors in laminar diffusion flames.

Zhao *et al.* [35] studied the OH formation in a hydrogen diffusion co-flow burner through chemiluminescence images and CFD simulations. The flow conditions were fixed with and without co-flow air with a central hydrogen jet of D=15 mm and low thermal powers (~0.2 kW). The numerical results showed a flame height of ~20 mm and were in good agreement with the experimental measurements. The numerical results showed slightly longer flames for the case with co-flow air as well as higher maximum temperature. This could be attributed to the higher inlet thermal power used in the flame with co-flow air.

Li *et al.* [36] experimentally and numerically investigated the combustion and heat release characteristics of a hydrogen laminar diffusion flame in a non-premixed micro-jet burner (1 mm diameter for H_2 inlet and 3.16 mm for air) together with OH distribution measurements at various inlet powers (from 0.1 kW to 1.0 kW) and equivalence ratios. The flame structure was obtained by flame image detection and spectroscopic systems. However, NO_x emissions were not measured in this work. Laminar flames were studied varying the inlet hydrogen Reynolds number between 14 and 144, while the Reynolds number of the inlet air flows varied between 2 and 52. Their experimental and numerical results showed longer flames for higher inlet powers, whereas different equivalence ratios would lead to similar flame volumes at a given inlet power.

Khan and Raghavan [37] investigated non-premixed laminar jet flames using carbon monoxide-hydrogen mixtures. Varying the inlet composition, they carried out a numerical and experimental analysis of the flame length, thermal plume width, temperature and flame luminosity. They concluded that the flame became shorter as hydrogen content was increased and that thermal plume width got wider. In addition, when adding hydrogen to the inlet mixture, the maximum temperature isotherm moved closer to the burner exit (moving the reaction volume to a zone of shorter residence times τ_{res}), but also showing an increasing trend in the maximum temperature (and therefore possibly higher $\dot{\omega}_{NOx}$).

In this paper, we present the results of experiments in a coaxial H_2/air burner at low Reynolds number in order to study possible flame splitting strategies for NO_x reduction in domestic boiler burners. The different flames are modelled numerically in order to further analyse the results observed experimentally and better understand the different trends in thermal NO_x concentrations depending on inlet power and equivalence ratio. Following the ideas suggested by Peters *et al.* [34], the numerical results are used to extract the thermal NO_x reaction volume $\mathcal{V}_{reac}$ and a weighted average $\overline{\dot{\omega}_{NO}}$ indicating the competition between residence time τ_{res} and chemical reaction time $1/\dot{\omega}_{NO}$ within $\mathcal{V}_{reac}$. In the light of this discussion of the measured NO_x trends, different strategies are discussed for the design of low NO_x hydrogen diffusion burners. Finally, the effect of coaxial air on NO_x reduction compared to a simple jet flame is illustrated in the appendix.

2. Aims and Methodology

2.1. Single-burner experimental configuration

The flame under study was defined as a single flame from an hypothetical array burner, as illustrated in Figure 1. The conceptual design of such burner is based on the patent developed by *IK4-Ikerlan* [38]. Future steps in the design methodology would involve the geometry optimization of the inlet jets, the interaction between several flames and the design optimization for burner integration in real boiler operating conditions.
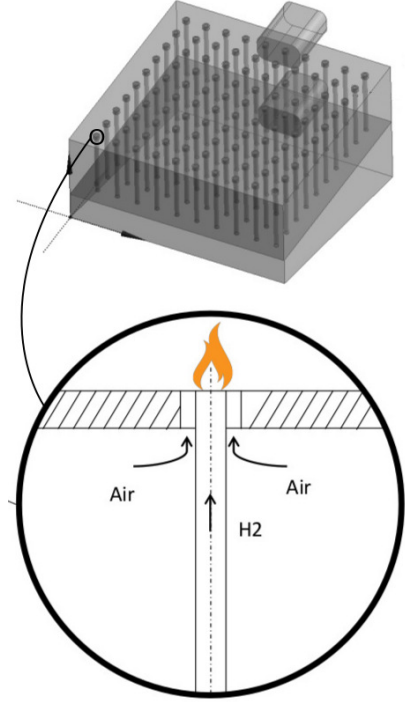

Figure 1: Single flame from an hypothetical array burner.

It can be noted that air is coaxially introduced to guarantee hydrogen combustion within the chamber. Coaxial air introduction and low fuel-air ratios have been characterized as a good alternative to reduce NO_x formation in turbulent non-premixed flames [33, 39, 40] (in the last parts of this paper, we will propose some possible explanations for such observations: shorter and narrower flames when coaxial air is introduced and lower spreading angles of the jet flames at lower fuel-air ratios, both implying smaller reaction volumes). However, these alternatives have been hardly studied for laminar non-premixed hydrogen flames. In the present work, the effect of fuel-air ratio on NO_x formation is studied for $\phi = 0.91$, $\phi = 0.83$ and $\phi = 0.77$, where ϕ is an equivalence ratio based on the injected mass flow rates of fuel and coaxial air. We considered values of $\phi < 1$, relevant for domestic gas boiler burners.

In addition, the flame splitting method similar to the study of Igawa *et al.* [31] is analyzed by varying the flame power from 0.2 to 1.0 kW, corresponding to increasing inlet mass flow rates. Design limits are imposed by considering a domestic burner of 20 kW. For example, if individual flames of 1.0 kW were selected as the best choice, the burner would require an array of

20 flames to cover the maximum power level. For lower thermal loads (e.g. 5 kW) each flame would work with an inlet power of 0.25 kW. The single flame study was carried out in the cylindri-
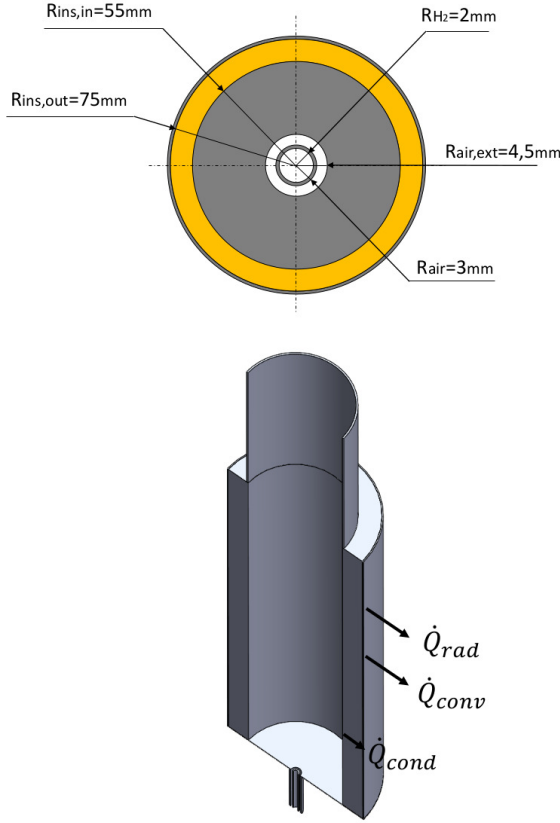

Figure 2: Combustor geometry showing the most relevant dimensions and heat transfer mechanisms across the walls considered

cal combustor shown in Figure 2. The most relevant dimensions are shown in the upper view, with the yellow surface referring to the insulation. The total length of the combustor is 300 mm.

Moreover, in order to obtain temperature measurements, an unconfined flame configuration was also considered with the same coaxial burner, without the cylindrical combustion chamber.

As discussed at the end of this paper, the analysis of NO_x formation trends in this single flame configuration is useful in order to identify key design aspects for low NO_x hydrogen diffusion array burners, and consider different design strategies depending on the burner regime (laminar/turbulent).

2.2. Numerical set-up

In order to reduce the computational costs, 2D axisymmetric geometries were used. As previously mentioned, the numerical results were used to understand the NO_x formation trends, extracting the thermal NO_x reaction volume $\mathcal{V}_{reac}$ and studying the competition between residence time τ_{res} and chemical reaction time $1/\dot{\omega}_{NO}$ within $\mathcal{V}_{reac}$.

A grid independence study was conducted considering three structured meshes. Table 1 summarises the characteristics of

Table 1: Number of cells for the three grids considered: number of cells in the radial direction in the H_2 inlet pipe (N_{H_2}), above the burner rim (N_{rim}) and in the coaxial air pipe (N_{air}), and total number of elements in the grids. Obtained maximum temperature values and NO_x concentrations for three grids in the case 0.4 kW, $\phi = 0.83$

	N_{H_2}	N_{rim}	N_{air}	Elements	T_{max} [K]	NO_x [ppm]
Grid 1	8	4	6	50752	2365	84
Grid 2	12	6	9	114192	2368	88
Grid 3	20	10	15	317200	2368	88

each grid. Each grid was constructed in the same way, with a similar cell distribution. The smallest grid size in the domain is the same uniform grid size used in the radial direction to discretize the fuel and coaxial air inlet pipes together with the burner rim (implying the number of cells in each of these zones reported in Table 1). At the burner exit, the grid size in the axial direction is specified as twice this smallest grid size. The grids are stretched both in the radial direction (from the coaxial air edge to the insulation) and in the axial direction. Grid 2, shown in Figure 3, proved to be sufficiently accurate to ensure grid-independent solutions and all the calculations presented in the following are performed on this grid.
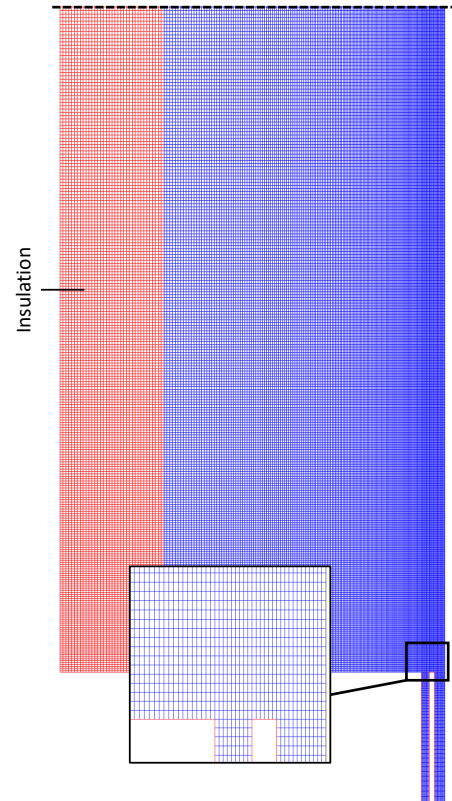

Figure 3: General and detailed view of the selected mesh (Grid 2).

A no-slip condition was imposed at the burner walls, with the first normal derivatives of species mass fractions set to zero. It can be noted that the conductive heat transfer along the insu-

lation was also modelled. In addition, combined heat transfer (convection+radiation) was taken into account at the external combustion chamber wall.

Numerical simulations were carried out using the software ANSYS Fluent 2019 R3 [32], which employs a Finite-Volume Method to solve the equations for the conservation of mass, momentum, energy and species. The discretized convective terms of the mentioned conservation equations were solved using a second-order upwind scheme, while gradients were evaluated through the Least Squares method. Pressure-velocity coupling was solved using the coupled algorithm. Additional simulations
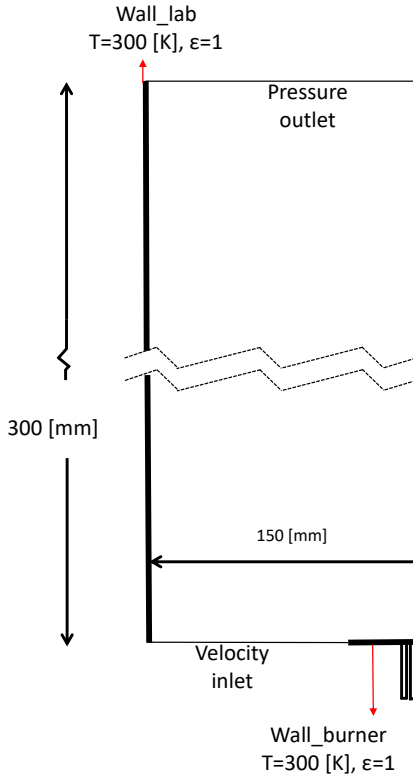

Figure 4: 2D axisymmetric geometry for the unconfined flame.

were carried out in order to reproduce the unconfined flame. The obtained comparative results could then be used to understand and explain the main results of the confined flame since identical models and solver schemes were used in both confined and unconfined simulations. The boundary conditions for the unconfined flame model are shown in Figure 4, with the laboratory and burner base walls defined as black bodies at T_{inf}=300 K.

3. Experimental measurements

3.1. NO_x emission measurements

The main components of the experimental setup are shown schematically in Figure 5. Hydrogen is supplied from a high pressure steel container and compressed air is taken from the compressed air line. The flow rates are controlled by mass flow
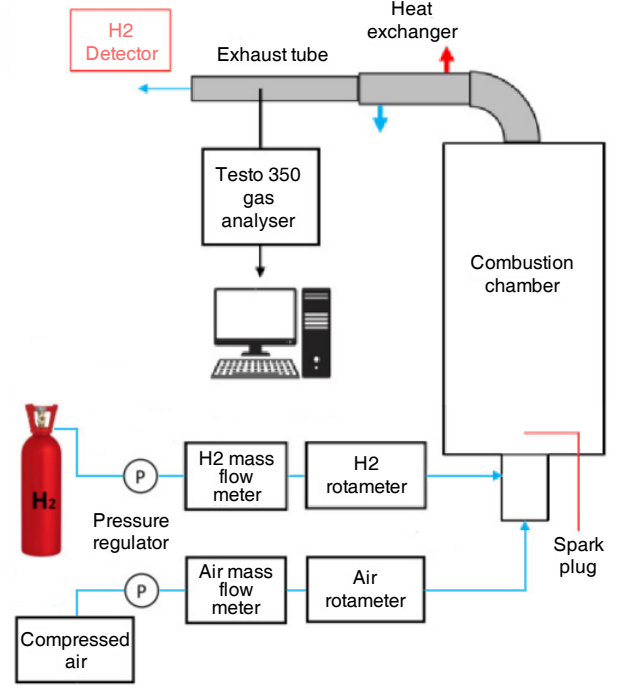

Figure 5: Experimental setup scheme

controllers, and can be varied between 0-10 L/min for hydrogen and 0-20 L/min for air. Those mass flow controllers are connected to a Brooks 0152 Microprocessor control&read out unit® in order to control the fixed mass flow values manually. Additionally, the mass flow values are verified using two rotameters for hydrogen and air. Pressure regulators are employed to fix hydrogen and air pressures at 2 and 5 bar respectively.

The cylindrical combustion chamber shown in Figure 6 was fabricated with AISI 316L steel and painted with high temperature thermographic spray paint. The chamber dimensions are those shown in Figure 2. A tubular water heat exchanger was used to cool the exhaust gases. Once cooled, the NO_x and oxygen levels were measured using a Testo 350® gas analyzer on a dry basis and corrected to 0% O_2. In addition, measurements were carried out with an hydrogen detector located downstream the outlet in order to ensure safe operating conditions. Each measurement was maintained for five minutes to ensure steady state.

3.2. Axial temperature measurements

Since temperature is one of the most critical variables for thermal NO_x formation, axial temperatures were measured at different locations along the axis using a Pt-6%Rh/Pt-30%Rh (B-type) thermocouple as shown in Figure 7. An adjustable controlled mechanism was used to move the thermocouple vertically, allowing displacements of 1 mm. The measured signals were processed with Agilent 34972A® data logger. Temperature readings at each height presented fluctuations of about ±15°C and were averaged by measuring on intervals of 180s. It can be seen that the combustion chamber was removed to

Figure 6: Experimental combustion chamber.

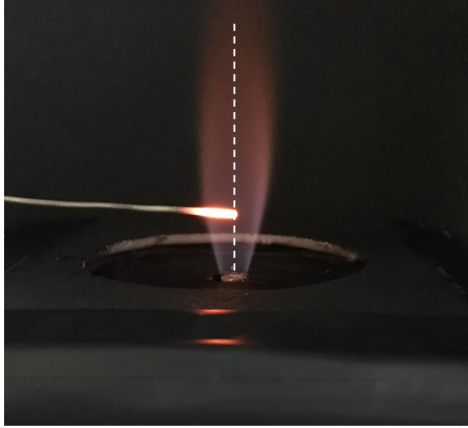permit the measurements and to control the axial position with the motorized mechanism.

Figure 7: Axial temperature measurements in the unconfined hydrogen flame.

Finally, the measured temperatures were corrected following the procedure of Bradley and Matthews [41]. Applying an energy balance from Equation (1) at the thermocouple tip, gas temperature was estimated following an iterative calculation.

$$h(T_{\text{flame}} - T_{\text{tc}}) = \epsilon_{\text{tc}}\sigma(T_{\text{tc}}^4 - T_{\text{inf}}^4) \qquad (1)$$

The mean thermocouple emissivity ϵ_{tc} was characterized by changing the emissivity of the thermal camera FLIR ThermaCam P25® until it matched the instantaneous temperature measurement of the thermocouple. A final value of $\epsilon_{\text{tc}} = 0.3$ was obtained. The heat transfer coefficient h was calculated from the Nusselt number, which was in turn calculated as a function of Reynolds number and Prandtl number. Following the same approach as in [42], temperature dependent values of mixture viscosity, conductivity, specific heat and density were taken from air properties. Also following [42], the Reynolds number was evaluated using the mean axial velocity taken from the

numerical results and introducing the thermocouple diameter (D =1.8 mm).

4. Modelling

The steady two-dimensional axisymmetric flow field was obtained by solving the exact Navier-Stokes equations. Moreover, species transport equations including chemical reaction source terms and the sensible enthalpy transport equation including a radiative heat loss source term were solved. We give here some details on the modelling of these source terms, together with the treatment of heat transfer within the insulation and through the outer boundary. The post-processing of the thermal NO_x is finally described.

4.1. Species transport and finite-rate chemistry

The steady-state convection-diffusion conservation equation for each species mass fraction Y_i can be written as:

$$\nabla \cdot (\rho \vec{v} Y_i) = -\nabla \cdot \overrightarrow{J_i} + R_i \qquad (2)$$

where $\vec{v}$ is the velocity vector obtained from the Navier-Stokes equations where the density ρ is obtained from the ideal gas law at atmospheric pressure.

The first term on the *R.H.S* (right-hand side) represents the species diffusive transport, which is particularly important in non-premixed flames. In particular in the case considered, where hydrogen diffuses much more rapidly than other molecules, the diffusive transport term should be properly modelled. Here, the full multicomponent diffusion [43, 44] is taken into account including thermal diffusive transport (Soret effect). Note that recent developments for a more efficient evaluation of the diffusion velocities [45] could be considered for future studies.

The last term on the *R.H.S* is the reactive term, which represents the formation and destruction rates of each specie i. The species mass fraction reaction rates $\dot{\omega}_i$ are obtained from the detailed mechanism of O'Conaire *et al.* [46], including 10 species (8 reacting species, plus N_2 and Ar) and 19 reactions.

The numerical resolution of (2) is done successively for each species i, where the convective and diffusion terms are treated implicitly, while the reactive terms are treated explicitly. In order to avoid convergence problems related to the possible stiffness of these explicit source terms, the approach used in ANSYS Fluent introduces an approximation that considers the effect of the reactive terms over small characteristic times τ, such that:

$$R_i = \frac{\rho}{\tau} \int_0^\tau \dot{\omega}_i dt \qquad (3)$$

This standard approximation used in ANSYS Fluent for stationary problems would deserve to be further investigated. Nevertheless, it proved to be sufficient for the present study.

4.2. Energy transport equation

The temperature was obtained by solving an energy transport equation in both fluid and solid regions.

Combustion chamber. The steady-state transport equation for sensible enthalpy reads:

$$\nabla \cdot (\rho \vec{v} h_s) = \nabla \cdot \left(k \nabla T - \sum_j h_j \vec{J_j} \right) + S_{\text{chem}} + S_{\text{rad}} \qquad (4)$$

The four terms on the *R.H.S* represent energy transfer due to thermal diffusion, enthalpy transport due to species diffusion, source of energy due to chemical reactions and radiation heat loss, where the conductivity of the gas mixture k was calculated using the Hirschfelder equation based on kinetic theory, and where h_i is the sensible enthalpy of species i. The radiation source term S_{rad} was calculated using the discrete ordinates (DO) method, which solves the radiative transfer equation for a finite number of discrete solid angles. In the present work four θ and φ divisions for the angular discretization were used, yielding to eight solid angles. The emittance of the H_2O molecules was calculated using the weighted-sum-of-gray-gases model (WSGGM), which expresses the total gas emittance as a weighted sum of gray gas emittances [47].

Heat conduction in outer insulation of the chamber. In the solid regions, enthalpy transport equation reduces to heat conduction (heat transfer referred to as $\dot{Q}_{\text{cond}}$ in Figure 2):

$$\nabla \cdot (k_w \nabla T) = 0 \qquad (5)$$

where the temperature dependent thermal conductivity k_w in the cylindrical insulation was obtained according to the data given by the provider of the insulation material.

Heat transfer at external combustor chamber wall. In order to model the heat exchange between combustor and ambient air, a combined heat transfer (convection+radiation) boundary condition was imposed at the external chamber wall (corresponding to $\dot{Q}_{\text{conv}}$ and $\dot{Q}_{\text{rad}}$ in Figure 2).

The convective heat transfer coefficient is given the fixed value $h_0 = 6.5$ W/m^{2}K, such that:

$$\dot{Q}_{\text{conv}} = h_0 \sum A_i (T_{w,i} - T_0) \qquad (6)$$

where A_i and $T_{w,i}$ are the grid cell surface area at the external wall and its temperature, respectively, and where T_0 is the temperature of the ambient air.

The value of the heat transfer coefficient h_0 was calculated using the following Nusselt number expression [14]:

$$Nu = \left[0.825 + \frac{0.387 Ra_L^{1/6}}{[1 + (0.492/Pr)^{9/16}]^{8/27}} \right]^2 \qquad (7)$$

where Ra_L is the Rayleigh number which is the product of the Grashof and Prandtl numbers [14]. Hence, the heat transfer coefficient h_0 can be calculated for each surface temperature from the definition of Nusselt number. The mean value of 6.5 was obtained by varying the temperature of the external wall from 320 K to 500 K.

Radiation heat loss from the external wall to the surrounding ambient air was modelled assuming diffusive grey surface and

fixing the surface emissivity at $\varepsilon = 0.98$. Such a high emissivity was achieved by painting the external wall of the experimental combustor with a matt nitroalkydale black spray, which increases the emissivity of the painted surface. The value 0.98 was experimentally obtained by heating the wall and measuring the temperature using a surface thermocouple and FLIR ThermaCam P25$^\circledR$ infrared thermal camera. The emissivity of the thermal camera was changed until it was equal to the instantaneous temperature measurement of the thermocouple.

With these parameters, the radiative heat transfer between the external wall and the environment was modelled as:

$$\dot{Q}_{\text{rad}} = \varepsilon \sigma \sum A_i (T_{w,i}^4 - T_0^4) \qquad (8)$$

where $\sigma = 5.67 \times 10^{-8}$ W/(m^2 K^4) is the Stephan-Boltzman constant.

4.3. Thermal NO$_x$ post-processing

The main objective of the study is to analyze the effect of inlet power and equivalence ratio on NO$_x$ formation. As there are no CH radicals and pressures are relatively low, prompt NO$_x$ and nitrous oxide NO$_x$ mechanisms are neglected. Since thermal NO$_x$ emissions mainly consist of nitric oxide [15, 25, 48], its formation is modelled using the well known Zeldovich mechanism formed by three elementary reactions, assuming that all NO$_x$ is NO generated by the thermal NO$_x$ mechanism:

$$O + N_2 \leftrightarrows N + NO \qquad (9)$$
$$N + O_2 \leftrightarrows NO + O \qquad (10)$$
$$N + OH \leftrightarrows NO + H \qquad (11)$$

The name *thermal* is used due to the high activation energy of the reaction (9) caused by the triple bond in the N_2 molecule and is only sufficiently fast at high temperatures. Thus reaction (9) is the rate-limiting step of thermal NO formation due to its low rate [15].

In order to obtain accurate results, this mechanism could be accounted for by adding more elementary reactions to the detailed mechanism in (2) [49, 50]. However, this would increase the number of species to be transported as well as the solution matrix. Hence, NO$_x$ models are commonly decoupled from the main reaction mechanism, computing their reaction rates in a post-processing step through the converged temperature and species concentration values [51, 52, 53].

The calculation was carried out disabling the main equations (continuity, momentum, energy and main species transport) and solving the transport equation for Y_{NO}:

$$\nabla \cdot (\rho \vec{v} Y_{\text{NO}}) = \nabla \cdot (\rho D \nabla Y_{\text{NO}}) + \rho \dot{\omega}_{\text{NO}} \qquad (12)$$

where D is an effective diffusion coefficient and $\dot{\omega}_{\text{NO}}$ is the reactive source term calculated considering the above Zeldovich mechanism (9)-(11) with rate constants taken from the evaluation of Hanson and Salimian [54].

5. Experimental and numerical results

5.1. General observations

The power range under study was from 0.2 to 1.0 kW and consequently the inlet Reynolds numbers increased with increasing inlet mass flows rates. No steady solution could be obtained numerically when increasing the inlet power above 0.6 kW, suggesting that laminar-turbulent transition was reached. This non-laminar regime is observed experimentally in the unconfined flames at 0.8 kW as shown in Figure 8 for the case $\phi = 0.91$. Therefore, the computational study was limited to the range 0.2-0.6 kW while experimental measurements were maintained for the whole range (0.2-1.0 kW).
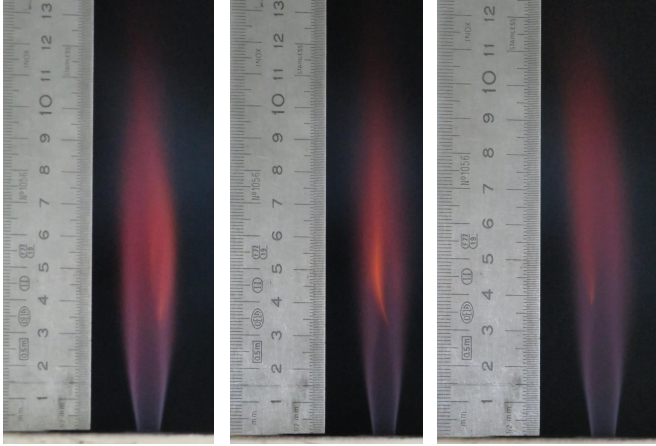

Figure 8: Image sequence illustrating the non-laminar regime of the unconfined flame at 0.8 kW and $\phi = 0.91$ (image sequence captured using a Canon EOS M50® camera at burst mode with 10 fps).

Different trends of NO_x concentrations will be observed in the following depending on whether laminar or non-laminar flames are considered. According to Chen and Driscoll [33], the differences in NO_x between laminar and turbulent regimes can be explained by considering reaction volumes $\mathcal{V}_{reac}$, residence times τ_{res} and NO_x chemical times $1/\dot{\omega}_{NOx}$. It will be useful to consider the relative importance of each factor in order to interpret the experimental and numerical results.

Before considering more detailed comparisons of temperatures and NO_x concentrations, we can observe in Figure 9 that a general good qualitative agreement is obtained between experimental and numerical results (here at equivalence ratio $\phi = 0.91$ in the unconfined configuration).

5.2. Temperature validation in unconfined configuration

Figure 10 shows a validation of axial temperature in the unconfined configuration for 0.2 kW at $\phi = 0.83$. A good agreement between simulation results and experimental data is observed, in particular at heights below x = 15 mm. It can also be observed that computational results slightly over-estimate the maximum temperature value (~54 K). On the one hand, discrepancies between measurements and modelling may be attributed to the uncorrected conduction losses along the thermocouple. In addition, experimental results were corrected
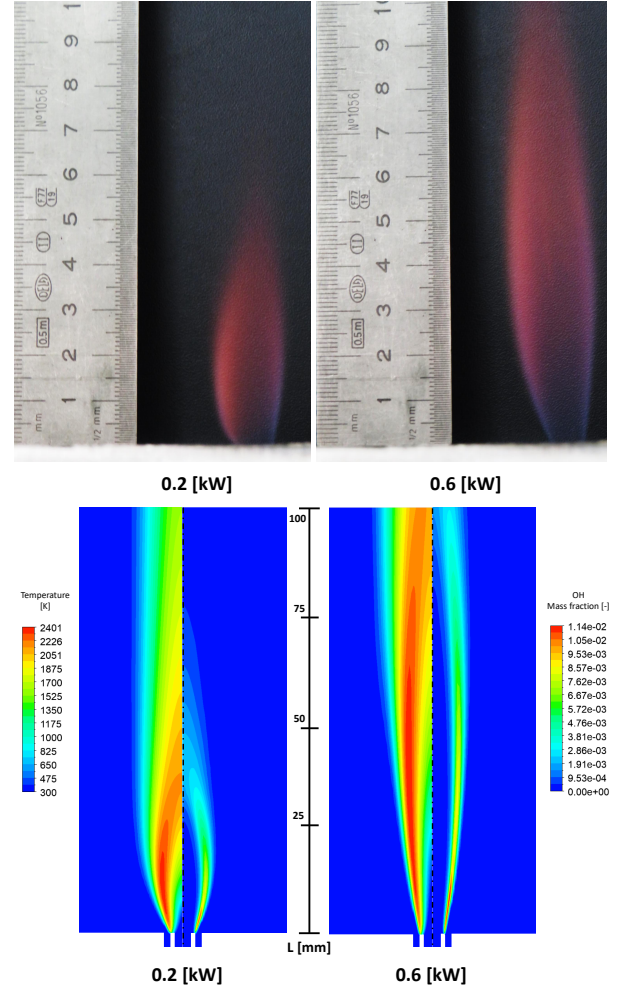

Figure 9: Pictures of unconfined flames for two inlet powers at $\phi = 0.91$ (top) and corresponding numerical results for temperature and OH mass fraction (bottom).

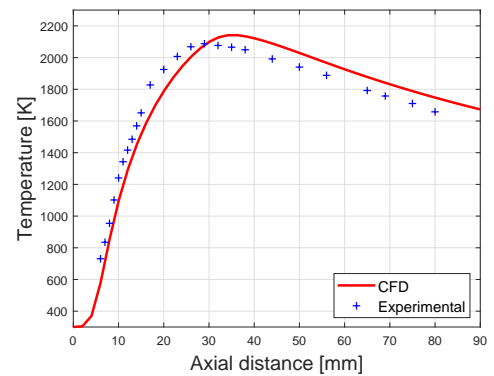Figure 10: Experimental and numerical axial temperatures (inlet power 0.2 kW, $\phi = 0.83$).

using the mixture properties of air, while the mean axial velocities were taken from the numerical results. On the other hand, the modelling assumptions and simplifications could be improved, both for the reactive source terms that use the approximation (3), and in the treatment of radiative heat transfer

8

using WSGGM with a finite number of discrete solid angles and boundary walls with constant temperature and emissivity. Still, the good agreement between numerical results and experimental data shown in Figure 10 for the unconfined configuration suggests that the proposed numerical modelling framework correctly captures the main physics of the laminar flames considered here.
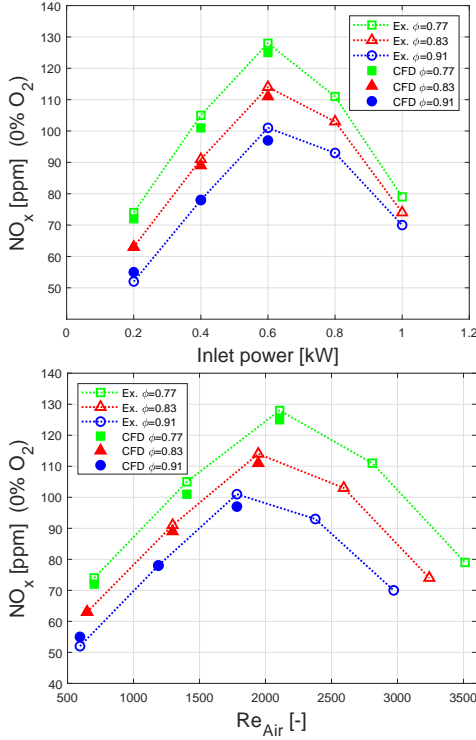
5.3. Thermal NO_x validation

Figure 11: Experimental and numerical NO_x concentrations for different equivalence ratios, as a function of inlet power (top) and as a function of the Reynolds number of the coaxial air stream (bottom).

Figure 11 shows the experimental and numerical NO_x concentrations for each equivalence ratio, as a function of inlet power (top figure) and as a function of the Reynolds number of the coaxial air stream (bottom figure). The agreement is good for the different laminar flames considered, and it can be seen that numerical NO_x results are able to predict the formation trends when increasing the inlet power, with a maximum value at 0.6 kW. The experimental results show decreasing NO_x concentrations for inlet power of 0.8 and 1.0 kW (corresponding to values of Re_{Air} above 2000), confirming a transition from laminar to turbulent above inlet powers of 0.6 kW.

6. Discussion

Different trends have been observed in the results. NO_x concentrations increase with inlet power in the laminar regime, while the opposite trend is observed experimentally when flames are not laminar. On the other hand, NO_x concentrations are higher at lower equivalence ratios, even out of the laminar

regime. Since the numerical results correctly capture the main features of the flames considered, we will use them in order to interpret the trends in the laminar cases.
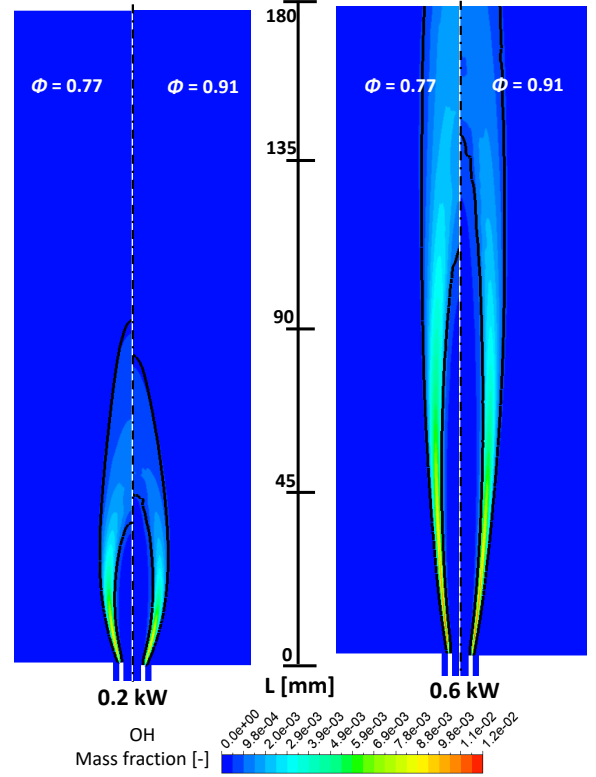

Figure 12: Contours of OH mass fraction at two inlet powers and two equivalence ratios, together with the isosurface $\dot{\omega}_{NO} = 0.1 s^{-1}$ defining $\mathcal{V}_{reac}$ (black line).

Some qualitative ideas on reaction volumes $\mathcal{V}_{reac}$, residence times τ_{res} and reaction times $1/\dot{\omega}_{NO}$ can already be extracted from Figures 12, 13 and 14. We will now try to consider these different factors in more detail.

6.1. Influence of inlet power

In order to quantify the volume $\mathcal{V}_{reac}$ where NO_x is produced, we simply extract the volume from the numerical results where the chemical reaction rate of NO is larger than a small number (for instance $\dot{\omega}_{NO} > 0.1 s^{-1}$):

$$\mathcal{V}_{reac} = \iiint_{[\dot{\omega}_{NO} > 0.1 s^{-1}]} d\mathcal{V} \tag{13}$$

This is the volume within the isosurface $\dot{\omega}_{NO} = 0.1 s^{-1}$ represented in Figure 12. Note that a definition could also be based on a high temperature region, since this is a necessary condition in order to activate the rate-limiting reaction (9), as previously explained. However, the above definition seems more appropriate by including all the factors describing a high NO production zone, since not only high temperatures, but also for instance relevant concentrations of O radicals are required for the activation of reaction (9).
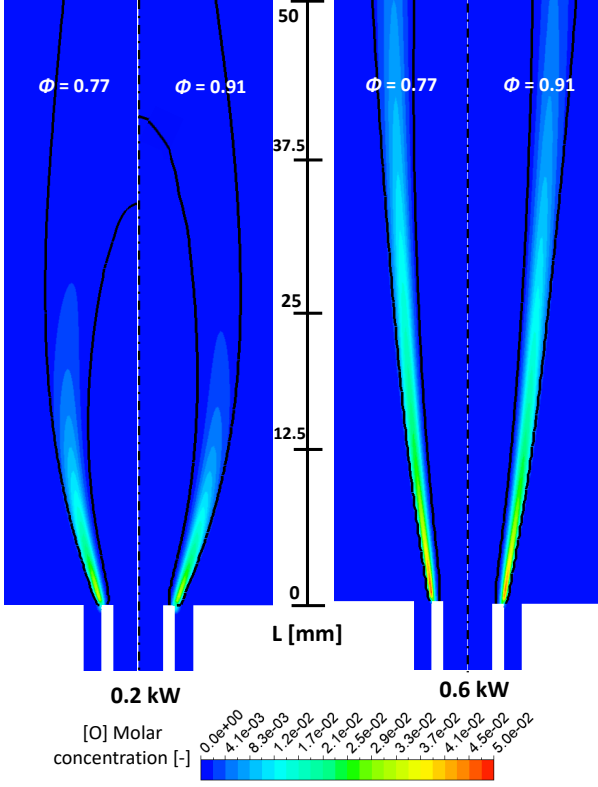
9

Figure 13: Contours of O concentrations at two inlet powers and two equivalence ratios, together with the isosurface $\dot{\omega}_{NO} = 0.1 s^{-1}$ defining $\mathcal{V}_{\text{reac}}$ (black line).

Figure 14: Contours of $\dot{\omega}_{\text{NO}}$ at two inlet powers and two equivalence ratios, together with the isosurface $\dot{\omega}_{NO} = 0.1 s^{-1}$ defining $\mathcal{V}_{\text{reac}}$ (black line).

As already discussed, the larger $\mathcal{V}_{\text{reac}}$, the larger the zone where NO_x is produced. However, the intensity of NO_x production should also be considered within $\mathcal{V}_{\text{reac}}$. This can be related to the competition between a residence time τ_{res} (which can be assumed to be inversely proportional to the velocity magnitude $|\vec{v}|$) and a chemical time (inverse of $\dot{\omega}_{\text{NO}}$). We can consider for instance the inverse-velocity weighted average of $\dot{\omega}_{\text{NO}}$ within $\mathcal{V}_{\text{reac}}$:

$$\overline{\dot{\omega}_{\text{NO}}} = \frac{\iiint_{[\mathcal{V}_{\text{reac}}]} \dot{\omega}_{\text{NO}} / |\vec{v}| \, d\mathcal{V}}{\iiint_{[\mathcal{V}_{\text{reac}}]} 1 / |\vec{v}| \, d\mathcal{V}} \tag{14}$$

which should give an idea of the intensity of NO_x production within $\mathcal{V}_{\text{reac}}$. The larger $\overline{\dot{\omega}_{\text{NO}}}$, the more intense the production of NO_x within $\mathcal{V}_{\text{reac}}$.

Figure 15 shows opposite effects for these two factors. On the one hand, the reaction volume increases with increasing inlet powers (longer laminar flames). On the other hand, $\overline{\dot{\omega}_{\text{NO}}}$ decreases (high reaction rates found in regions of shorter residence times). Hence, we can claim that the increasing NO_x concentrations with increasing inlet powers observed in Figure 11 in the laminar regime is mainly due to longer flames and therefore larger NO_x reaction volumes.

On the other hand, we can attribute the opposite trend observed experimentally for non-laminar flames to the less intense NO_x production within $\mathcal{V}_{\text{reac}}$. This is in line with the observations of Chen and Driscoll [33] for simple turbulent jet flames (without coaxial air) where flame lengths remain rather
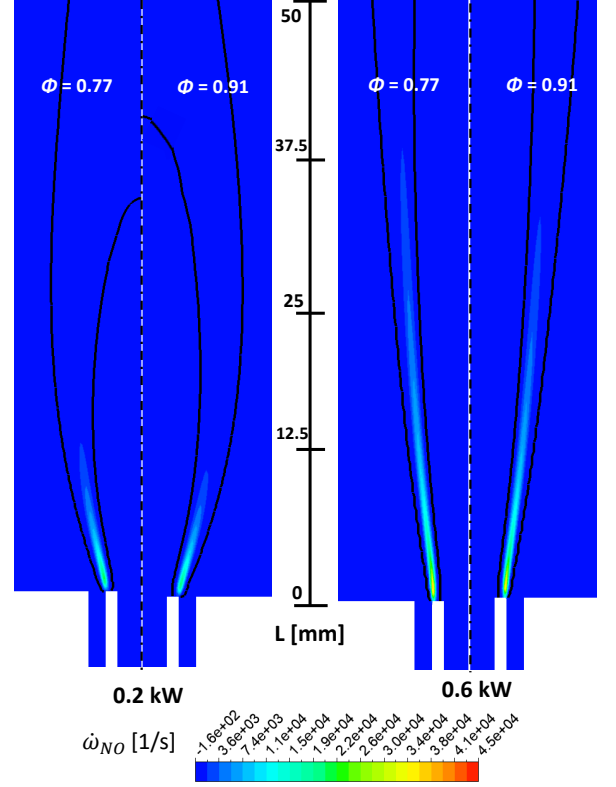
constants (implying constant flame volumes since $\mathcal{V}_{\text{reac}} \backsim L_f^2 . \delta$ [34]), whereas they increase for laminar flames. Moreover, in addition to shorter residence times, we could also expect lower local reaction rates $\dot{\omega}_{\text{NO}}$ at higher inlet powers in turbulent flames, related to higher local strain rates and more intense molecular mixing.

6.2. Influence of equivalence ratio

The trend of higher NO_x concentrations for lower equivalence ratios observed in Figure 11 is also explained by Figure 15. At low inlet powers, the reaction volumes are similar at all ϕ and the difference in NO_x concentration is directly explained by the higher reaction intensity at lower equivalence ratios. We can indeed expect higher local values of $\dot{\omega}_{\text{NO}}$ due to higher local concentrations of O when more coaxial air is injected.

With increasing inlet power, however, this difference is reduced (experimental curves are closer above 0.6kW in Figure 11 (top)) because of smaller reaction volumes at lower ϕ. We can see from Figure 14 that this is due to a lower spreading angle of the jet flames at lower ϕ (rather than shorter flames). This is in line with the observation of Chen and Driscoll [33] in fully turbulent flames where coaxial air reduced NO_x emission index. We can therefore expect that the three lines in the top plot of Figure 11 would cross for some inlet power values above 1.0 kW, implying NO_x reduction with lower ϕ values in fully turbulent flames as observed by Chen and Driscoll. However, in the low Reynolds number flames considered here, the
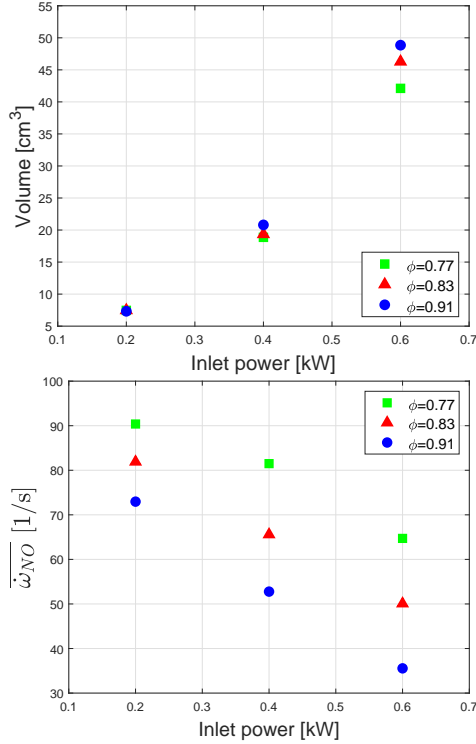
10

Figure 15: $\mathcal{V}_{\text{reac}}$ (top) and $\overline{\dot{\omega}_{\text{NO}}}$ (bottom) from the different laminar flame calculations.

opposite effect is observed: stronger coaxial air streams (lower equivalence ratios), implying higher local concentrations of O, enhance NO_x emissions, despite smaller reaction volumes and shorter residence times. Therefore, in contrast to previous non-premixed flame studies [33, 39, 40], it can be concluded that lower equivalence ratios promote the NO_x formation in laminar diffusion hydrogen flames with coaxially introduced air.

6.3. Low NOx domestic hydrogen burner design strategies

Considering the discussed results, two opposite strategies may be highlighted for the design of low NO_x hydrogen diffusion array burners depending on the flame regime.

Turbulent burners. A first strategy would consist in reducing the number of flames, implying higher thermal power and possibly fully turbulent flames with lower NO_x values. As previously discussed, we could indeed expect lower values of $\dot{\omega}_{\text{NO}}$ and shorter residence times, while reaction volumes $\mathcal{V}_{\text{reac}}$ would remain rather constant (expecting constant flame lengths L_f, with $\mathcal{V}_{\text{reac}} \backsim L_f^2.\delta$ [34]). Within the fully turbulent regime, equivalence ratio reduction and coaxial air introduction have already been considered as good alternatives to NO_x reduction [33, 39, 40].

For low power applications such as domestic boilers, a major drawback could be the need to considerably increase the volume of the combustion chamber due to the longer flames. Still, compact low emission turbulent burner designs could be based on flame aerodynamics, where several techniques such as cross flows, vortex generation, bluff bodies or swirling jets have

been successfully used [27, 55, 56]. Another issue for such turbulent domestic boilers would concern the maximum possible inlet mass flows (and therefore inlet Reynolds number), considering the limitations of the standard blowers used to suction the air into the chamber.

Laminar burners. A second opposite strategy would consist in increasing the number of flames in order to reduce the inlet power for each flame, ensuring a laminar regime where lower $\mathcal{V}_{\text{reac}}$ for each flame, would have a positive effect on NO_x reduction despite the increase of $\overline{\dot{\omega}_{\text{NO}}}$ as it has been already concluded from Figures 11 and 15. This is in line with the flame splitting method studied by Igawa *et al.* [31]. This approach would be more appropriate for domestic boilers or similar applications with spatial restrictions for burner integration in the overall system. In this case, we can expect an array burner with a large number of laminar flames of lower thermal power to reduce the NO_x concentrations, as we could observe at 0.2 kW, where the lowest NO_x concentrations were measured. As an example, considering a 20kW burner working at $\phi = 0.91$, 100 flames of 0.2kW would generate approximately 55 ppm of NO_x, while 34 flames of 0.6kW would generate about 100 ppm. Therefore the overall NO_x concentration would be reduced by $\backsim$ 45%. However the flame splitting method implies miniaturized air and hydrogen inlet holes, which could yield to complex geometries and manufacturing restrictions. In addition, further studies are required in order to verify that interactions between flames in an array burner do not alter the general observations made here on single burners.

7. Conclusions

Thermal NO_x formation in laminar H_2/air coaxial diffusion flames was analyzed through experimental measurements and CFD simulations. The influence of inlet power and equivalence ratio was experimentally and numerically analyzed varying the power from 0.2 to 1.0 kW at ϕ=0.77, 0.83 and 0.91. Numerical results were compared to axial temperature measurements for the unconfined flame, and to NO_x concentration measurements for the confined flame, showing satisfactory agreement in both cases. Using the validated CFD results, the different trends in NO_x concentrations depending on inlet power and equivalence ratio could be explained by considering different factors: a reaction volume $\mathcal{V}_{\text{reac}}$ and the competition between residence time τ_{res} and chemical reaction time $1/\dot{\omega}_{\text{NO}}$ within $\mathcal{V}_{\text{reac}}$. Moreover, the positive effect of coaxial air on NO_x reduction compared to a simple jet flame is also illustrated numerically in the Appendix.

In fully turbulent non-premixed hydrogen flames, low equivalence ratios can be used to reduce NO_x formation [33, 39, 40]. We observed the opposite effect in our laminar and low-Reynolds non-laminar flames, where higher NO_x concentrations were measured at lower equivalence ratios. The situation is indeed different than in fully turbulent flames, since the negative effects of lower Reynolds number (longer residence times) and larger reaction volumes (wider spreading angles of the jet

flames) at higher equivalence ratios are overruled by the positive effect of lower local NO_x reaction rates related to lower concentrations of O. Therefore, this study corroborates that near stoichiometric equivalence ratios would reduce NO_x formation in laminar flames.

Concerning the effect of inlet power on NO_x formation, a transition from laminar to turbulent was detected above 0.6 kW, were the NO_x formation trend is inverted. Therefore, considering the flame-splitting method for array-burner design, two opposite strategies may be considered for NO_x reduction: a reduced number of fully turbulent flames (with the possible drawback of too large combustion chambers for domestic boilers, and with inlet mass flow rate limitations due to the standard blowers used to suction the inlet air), or an increased number of laminar flames (with the possible manufacturing restrictions related to small inlets).

The insights gained from this study may be of assistance to the initial phase of a low NO_x hydrogen burner design. Likewise, this research has thrown up many questions in need of further investigation such as the influence of the interaction between several flames on NO_x formation or the parametric study of different burner geometries.

Acknowledgements

Appendix A. Effect of coaxial air on thermal NO_x

The effect of coaxial air on NO_x formation can also be analysed numerically. For that purpose, a flame at 0.4 kW is simulated without coaxial air (simple diffusion flame). Coflowing air is introduced as a low velocity stream (5% of the main jet velocity). Figure A.16 gives a qualitative picture of these results compared to the results of the confined flame at $\phi = 0.91$.

The OH mass fraction contours indicate a shorter, narrower and thinner flame in the confined coaxial air case. In order to quantify this effect, the volumes $\mathcal{V}_{\text{reac}}$ (defined here as $\dot{\omega}_{NO} > 5s^{-1}$) and the inverse-velocity weighted averages $\overline{\dot{\omega}_{NO}}$ are given in Table A.2.

Table A.2: Maximum temperature values, $\mathcal{V}_{\text{reac}}$, $\overline{\dot{\omega}_{NO}}$ and *EINOx* in two laminar flames with inlet power 0.4 kW: (a) a simple jet flame and (b) the confined flame with coaxial air (case $\phi = 0.91$).

Case	$T_{\max}$ [K]	$\mathcal{V}_{\text{reac}}$ [cm^3]	$\overline{\dot{\omega}_{NO}}$ [1/s]	*EINOx* [g NO_x /kg H$_2$]
(a)	2463	7.68	177.43	8.79
(b)	2372	4.89	110.68	2.16

The numerical results show that maximum temperature is 91 K lower in the coaxial air case, and we see a reduction of
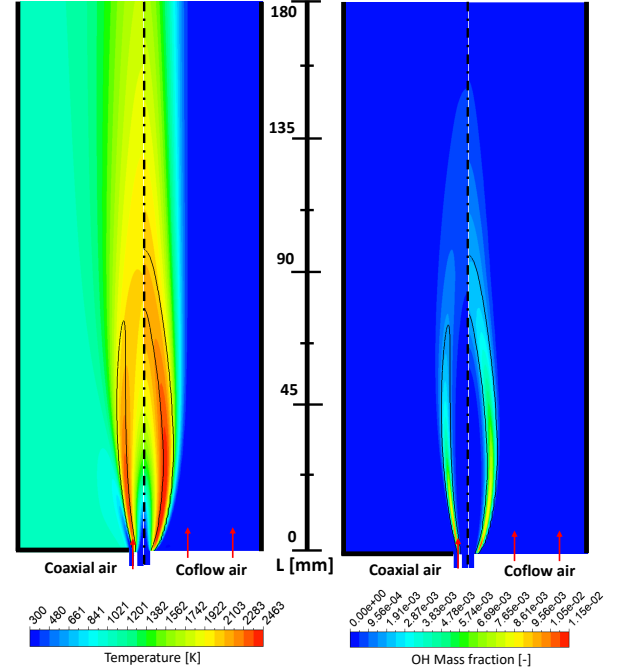

Figure A.16: Temperature and OH mass fraction contours at inlet power 0.4 kW, for the confined flame with coaxial air stream ($\phi = 0.91$) and a simple jet flame. The black line indicates the isosurface $\dot{\omega}_{NO} = 5s^{-1}$ (used to define $\mathcal{V}_{\text{reac}}$ in this case).

both $\mathcal{V}_{\text{reac}}$ and $\overline{\dot{\omega}_{NO}}$ (in line with shorter residence times). Consequently, as show in Table A.2, the *EINOx* (emission index of NO_x: grams of NO_x per kilograms of fuel) is reduced by approximately 75%, showing that coaxial air has a positive effect on NO_x reduction.

References

[1] M. Jacobson, Clean grids with current technology., Nature Energy 2016;6:441-442.

[2] Fuel Cells and Hydrogen Joint Undertaking, Hydrogen roadmap europe (2019). Onlyne database https://www.fch.europa.eu/news/hydrogen-roadmap-europe-sustainable-pathway- european-energy-transition [accessed 24/1/2020].

[3] P. E. V. de Miranda, Chapter 1 - hydrogen energy: Sustainable and perennial, in: P. E. V. de Miranda (Ed.), Science and Engineering of Hydrogen-Based Energy Technologies, Academic Press, 2019, pp. 1–38, doi:10.1016/B978-0-12-814251-6.00001-0.

[4] P. Nikolaidis, A. Poullikkas, A comparative overview of hydrogen production processes, Renewable and Sustainable Energy Reviews 2017;67:597–611, doi:10.1016/j.rser.2016.09.044.

[5] Z. Abdin, A. Zafaranloo, A. Rafiee, W. Mrida, W. LipiÅski, K. R. Khalilpour, Hydrogen as an energy vector, Renewable and Sustainable Energy Reviews 2020;120:109620, doi: 10.1016/j.rser.2019.109620.

[6] S. Khanmohammadi, M. Saadat-Targhi, Performance enhancement of an integrated system with solar flat plate collector for hydrogen production using waste heat recovery, Energy 2019;171:1066–1076, doi:10.1016/j.energy.2019.01.096.

[7] M. Deymi-Dashtebayaz, A. Ebrahimi-Moghadam, S. I. Pishbin, M. Pourramezan, Investigating the effect of hydrogen injection on natural gas thermo-physical properties with various compositions, Energy 2019;167:235–245, doi:10.1016/j.energy.2018.10.186.

[8] E. van der Roest, L. Snip, T. Fens, A. van Wijk, Introducing Power-to-H3: Combining renewable electricity with heat, water and hydrogen pro-

12

duction and storage in a neighbourhood, Appl. Energy 2020;257:114024, doi:10.1016/j.apenergy.2019.114024.

[9] X. Duan, Y. Li, J. Liu, G. Guo, J. Fu, Q. Zhang, S. Zhang, W. Liu, Experimental study the effects of various compression ratios and spark timing on performance and emission of a lean-burn heavy-duty spark ignition engine fueled with methane gas and hydrogen blends, Energy 2019;169:558–571, doi:10.1016/j.energy.2018.12.029.

[10] L. de Santoli, G. L. Basso, S. Barati, S. D'Ambra, C. Faso-lilli, Seasonal energy and environmental characterization of a micro gas turbine fueled with H2NG blends, Energy 2020;193:116678, doi:10.1016/j.energy.2019.116678.

[11] Y. Xiang, Z. Yuan, S. Wang, A. Fan, Effects of flow rate and fuel/air ratio on propagation behaviors of diffusion H2/air flames in a micro-combustor, Energy 2019;179:315-322, doi:10.1016/j.energy.2019.05.052.

[12] P.-G Aleiferis, M. Rosati, Controlled autoignition of hydrogen in a direct-injection optical engine, Combust. Flame 2012;159:2500–2515, doi:10.1016/j.combustflame.2012.02.021.

[13] I. Glassman, R. Yetter, N. Glumac, Combustion: Fifth Edition, Elsevier, Netherlands, 2014.

[14] Heat Transfer: A Practical Approach, no. v. 2 in Heat Transfer: A Practical Approach, McGraw-Hill, 2003.

[15] J. Warnatz, U. Maas, R. Dibble, Combustion - Physical and Chemical Fundamentals, Modeling and Simulation, Experiments, Pollutant Formation, Springer, 1996.

[16] A.L. Sánchez, F.A. Williams. Recent advances in understanding of flammability characteristics of hydrogen, Prog. Energy Combust. Sci. 2014;41:1–55, doi:10.1016/j.pecs.2013.10.002.

[17] H. de Vries, A. V. Mokhov, H. B. Levinsky, The impact of natural gas/hydrogen mixtures on the performance of end-use equipment: Interchangeability analysis for domestic appliances, Appl. Energy 2017;208:1007–1019, doi:10.1016/j.apenergy.2017.09.049.

[18] H. de Vries, H. B. Levinsky, Flashback, burning velocities and hydrogen admixture: Domestic appliance approval, gas regulation and appliance development, Appl. Energy 2020;259:114116, doi:10.1016/j.apenergy.2019.114116.

[19] M. A. Nemitallah, B Imteyaz, A Abdelhafez, M. A. Habib, Experimental and computational study on stability characteristics of hydrogen-enriched oxy-methane premixed flames, Appl. Energy 2019;250:433–443, doi:10.1016/j.apenergy.2019.05.087.

[20] A. C. Benim, K. J. Syed, Chapter 6 - flashback due to combustion instabilities, in: A. C. Benim, K. J. Syed (Eds.), Flashback Mechanisms in Lean Premixed Gas Turbine Combustion, Academic Press, Boston, 2015, pp. 41–44, doi:10.1016/B978-0-12-800755-6.00006-4.

[21] B. Gelfand, M. Silnikov, S. Medvedev, S. Khomik, Thermo-Gas Dynamics of Hydrogen Combustion and Explosion, Springer, 2012.

[22] Y. Zhao, S. Choudhury, V. McDonell, Influence of Renewable Gas Addition to Natural Gas on the Combustion Performance of Cooktop Burners, ASME 2018 International Mechanical Engineering Congress and Exposition (2018) V08AT10A012-V08AT10A012, doi:10.1115/IMECE2018-87932.

[23] S. Chodhury, V. McDonell, S. Samuelsen, Combustion performance of low-NOx and conventional storage water heaters operated on hydrogen enriched natural gas, Int. J. Hydrogen Energy 2020;45(3):2405-2417, doi:10.1016/j.ijhydene.2019.11.043.

[24] S. McAllister, J. Chen, A. Fernandez-Pello, Fundamentals of Combustion Processes, Mechanical Engineering Series, Springer New York, 2011.

[25] N. Peters, Turbulent Combustion, Press Syndicate of the University of Cambridge, The Pitt Building, Trumpington Street, Cambridge (UK), 2000.

[26] M. Skottene, K. E. Rian, A study of NO_x formation in hydrogen flames, Int. J. Hydrogen Energy 2007;32(15):3572-3585, doi:10.1016/j.ijhydene.2007.02.038.

[27] Z. Fu, H. Gao, Z. Zeng, J. Liu, Q. Zhu, Generation characteristics of thermal NOx in a double-swirler annular combustor under various inlet conditions, Energy 2020;200:117487, doi:10.1016/j.energy.2020.117487.

[28] G. Lopez-Ruiz, A. Fernandez-Akarregi, L. Diaz, I. Urresti, I. Alava, J. Blanco, Numerical study of a laminar hydrogen diffusion flame based on the non-premixed finite-rate chemistry model; thermal NOx assessment, Int. J. Hydrogen Energy 2019;44(36):20426-20439, doi:10.1016/j.ijhydene.2019.05.230.

[29] M. Ditaranto, T. Heggset, D. Berstad, Concept of hydrogen fired gas turbine cycle with exhaust gas recirculation: Assessment of process performance, Energy 2020;192:116646, doi:10.1016/j.energy.2019.116646.

[30] S. H. Pourhoseini, A novel configuration of natural gas diffusion burners to enhance optical, thermal and radiative characteristics of flame and reduce NOx emission, Energy 2017;132:41–48, doi:10.1016/j.energy.2017.04.167.

[31] S. Igawa, T. Matsui, A. Seo, NOx emission reduction in hydrogen combustion, International Gas Research Conference Proceedings 2011;2:1111–1125.

[32] ANSYS Fluent Inc., 2019R3, Documentation User's Guide, 2019.

[33] R.-H. Chen, J. F. Driscoll, Nitric oxide levels of jet diffusion flames: Effects of coaxial air and other mixing parameters, Symposium (International) on Combustion 1991;23 (1):281–288, Twenty-Third Symposium (International) on Combustion, doi:10.1016/S0082-0784(06)80271-7.

[34] N. Peters, S. Donnerhack, Structure and similarity of nitric oxide production in turbulent diffusion flames, Symposium (International) on Combustion 1981;18(1):33–42, Eighteenth Symposium (International) on Combustion, doi:10.1016/S0082-0784(81)80008-2.

[35] M. Zhao, D. Buttsworth, R. Choudhury, Experimental and numerical study of OH chemiluminescence in hydrogen diffusion flames, Combust. Flame 2018;197:369–377, doi:10.1016/j.combustflame.2018.08.019.

[36] J. Li, H. Huang, N. Kobayashi, Hydrogen combustion as a thermal source, Energy Procedia 2017;142:1083–1088, proceedings of the 9th International Conference on Applied Energy, doi:10.1016/j.egypro.2017.12.360.

[37] N. Khan, V. Raghavan, Structure and reaction zones of hydrogen carbon-monoxide laminar jet diffusion flames, Int. J. Hydrogen Energy 2014;39(34):19832–19845, doi:10.1016/j.ijhydene.2014.09.165.

[38] R. Marin Marin, L. Diaz Lecumberri, I. Urresti Ugarteburu, Gas burner, Applicant: Ikerlan S.Coop, Patent Number: EP3336427 (A1) (june 2018).

[39] S. Noda, J. Inohae, Z. S. Saldi, NOx emission characteristics of confined jet nonpremixed flames, Proceedings of the Combustion Institute 2007;31(1):1625–1632, doi:10.1016/j.proci.2006.07.088.

[40] J. Hwang, K. Sohn, N. Bouvet, Y. Yoon, NOx scaling of syngas H2/CO turbulent non-premixed jet flames, Combustion Science and Technology 2013;185(12):1715–1734, doi:10.1080/00102202.2013.831847.

[41] D. Bradley, K. Matthews, Measurement of high gas temperatures with fine wire thermocouples, Journal of Mechanical Engineering Science, 1968, doi:10.1243/JMES_JOUR_1968_010_048_02.

[42] H. Xu, F. Liu, S. Sun, Y. Zhao, S. Meng, W. Tang, Effects of H2O and CO2 diluted oxidizer on the structure and shape of laminar coflow syngas diffusion flames, Combust. Flame 2017;177:67–78, doi:10.1016/j.combustflame.2016.12.001.

[43] Hirschfelder, J.O., Curtiss, C.F., Bird, R.B., The Molecular Theory of Gases and Liquids, Wiley, New York NY, 1964.

[44] Dixon-Lewis, G., Flame structure and flame reaction kinetics II. Transport phenomena in multicomponent systems, Proc. Roy. Soc. A. 1968;304:111–135, doi:10.1098/rspa.1968.0178.

[45] Naud, B., Arias-Zugasti, M., Accurate multicomponent Fick diffusion at a lower cost than mixture-averaged approximation: validation in steady and unsteady counterflow flamelets, Combust. Flame 2020;219:120–128, doi:10.1016/j.combustflame.2020.05.003.

[46] M. O'Conaire, H. J. Curran, J. M. Simmie, W. J. Pitz, C. K. Westbrook, A comprehensive modeling study of hydrogen oxidation, Int. J. Chemical Kinetics 2004;36(11):603–622, doi:10.1002/kin.20036.

[47] H. Hottel, W. Hawthorne, Diffusion in laminar flame jets, Symposium on Combustion and Flame, and Explosion Phenomena 1948:3(1): 254–266, Third Symposium on Combustion and Flame and Explosion Phenomena, doi:10.1016/S1062-2896(49)80034-1.

[48] C. K. Law, Combustion Physics, Cambridge University Press, 2006.

[49] Y. Kang, S. Wei, P. Zhang, X. Lu, Q. Wang, X. Gou, X. Huang, S. Peng, D. Yang, X. Ji, Detailed multi-dimensional study on NOx formation and destruction mechanisms in dimethyl ether/air diffusion flame under the moderate or intense low-oxygen dilution (MILD) condition, Energy 2017;119:1195–1211, doi:10.1016/j.energy.2016.11.070.

[50] A. Frassoldati, T. Faravelli, E. Ranzi, A wide range modeling study of NOx formation and nitrogen chemistry in hydrogen combustion, Int. J. Hydrogen Energy 2006;31(15):2310–2328, doi:10.1016/j.ijhydene.2006.02.014.

[51] C. Schluckner, C. Gaber, M. Landfahrer, M. Demuth, C. Hochenauer, Fast and accurate CFD-model for NOx emission prediction during oxy-

fuel combustion of natural gas using detailed chemical kinetics, Fuel 2020;264:116841, doi:10.1016/j.fuel.2019.116841.

[52] W. P. Adamczyk, B. Isaac, J. Parra-Alvarez, S. T. Smith, D. Harris, J. N. Thornock, M. Zhou, P. J. Smith, R. Żmuda. Application of LES-CFD for predicting pulverized-coal workingconditions after installation of NOx control system, Energy 2018;160:693–709, doi:10.1016/j.energy.2018.07.031.

[53] S. Hill, L. D. Smoot, Modeling of nitrogen oxides formation and destruction in combustion systems, Prog. Energy Combust. Sci. 2000;26(4):417–458, doi:10.1016/S0360-1285(00)00011-3.

[54] R. K. Hanson, S. Salimian, Survey of Rate Constants in the N/H/O System, Springer New York, New York, 1984;361–421.

[55] J. M. Beer, Combustion Aerodynamics, Robert E. Krieger publishing company inc., Malabar, Florida, 1972.

[56] H. H. Funke, J. Dickhoff, J. Keinz, A. H. Ayed, A. Parente, P. Hendrick, Experimental and Numerical Study of the Micromix Combustion Principle Applied for Hydrogen and Hydrogen-Rich Syngas as Fuel with Increased Energy Density for Industrial Gas Turbine Applications, Energy Procedia 2014;61:1736–1739, doi:10.1016/j.egypro.2014.12.201.